© 2013. This manuscript version is made available under the CC-BY-NC-ND 4.0 license http://creativecommons.org/licenses/by-nc-nd/4.0/
The final version is available at https://doi.org/10.1016/j.matchemphys.2013.08.050

Formation and Stability of small well-defined Cu- and Ni oxide particles

Ramona Thalinger[1], Marc Heggen[2], Daniel G. Stroppa[2], Michael Stöger-Pollach[3], Bernhard Klötzer[1], Simon Penner[1]*

[1]Institute of Physical Chemistry, University of Innsbruck, A-6020 Innsbruck

[2]Ernst Ruska Zentrum und Peter Grünberg Institut, Forschungszentrum Jülich GmbH, 52425 Jülich, Germany

[3]University Service Facility for Transmission Electron Microscopy (USTEM), Vienna University of Technology, A-1040 Vienna

Corresponding author: S. Penner, Tel: 00435125075056 Fax: 00435125072925, simon.penner@uibk.ac.at

Keywords: oxidation, copper oxide, nickel oxide, electron microscopy, diffraction, HAADF

Abstract

Well-defined and –structured Cu/Cu_2O and Ni/NiO composite nanoparticles have been prepared by physical-vapor deposition on vacuum-cleaved NaCl(001) single crystal facets. Epitaxial growth has been observed due to the close crystallographic matching of the respective cubic crystal lattices. Distinct particle morphologies have only been obtained for the Ni/NiO particles, comprising truncated half-octahedral, rhombohedral- and pentagonal-shaped outlines. Oxidation of the particles in the temperature range 473-673 K in both cases led to the formation of well-defined CuO and NiO particles with distinct morphologies. Whereas CuO possibly adopts its thermodynamical equilibrium shape, NiO formation is accompanied by entering a Kirkendall-like state, that is, a hollow core-shell structure is obtained. The difference in the formation of the oxides is also reflected by their stability under reducing conditions. CuO transforms back to a polycrystalline mixture of Cu metal, Cu_2O and CuO after reduction in hydrogen at 673 K. In contrast, as expected from theoretical stability considerations, the formation of the hollow NiO structure is reversed upon annealing in hydrogen at 673 K and moreover results in the formation of a Ni-rich silicide structure Ni_3Si_2. The discussed systems present/exemplified a convenient way to tackle and investigate various problems in nanotechnology or catalysis, including phase transformations, establishing structure/activity relationships or monitoring intermetallic particles, starting from well-defined and simple models.

1. Introduction

Metal oxides are of paramount importance in many rapidly developing research areas such as the intersection of chemistry, physics and materials science [1]. Potential applications include sensors, microelectronics, corrosion protection coatings, fuel cells, nanotechnology in general or catalysis [1,2]. Focussing on the latter, oxides are widely used either as supports for catalytically active noble metals or as catalysts themselves [1,2]. However, while the catalytic action of noble metal particles is widely understood, several drawbacks in the use of oxides exist: due to their inherently more complex chemical nature, the catalytic action might depend on a number of factors, such as oxidation state, surface termination, polymorphism or the presence of oxygen defects [1]. Among the most widely used and characterized systems are the metals copper and nickel, as well as their corresponding oxides [3-5]. Here, the complexity manifests itself on the one hand by the presence of two important stable oxides with different properties for the copper system, that is, Cu_2O and CuO [6] and, on the other hand, by the stability of the NiO phase in hydrogen and the associated presence of defects in the NiO structure [7]. In turn, all three of them are of central importance in catalysis as they are used in various reactions like CO oxidation [8-11], methane steam reforming [12-14], CO_2 methanation [15,16], methanation of CO [7] or N_2O dissociation [7]. As the use of a structurally well-defined system is therefore imperative, lots of effort has especially been put into the understanding of the formation of CuO or Cu_2O following different oxidative or reductive preparation routines. This has already been scrutinized in a number of papers, also focusing on the comparison between bulk samples as well as nanoparticles and between different experimental conditions [17-21]. Formation of Cu_2O or CuO depending on oxygen partial pressure on bulk Cu has been reported [17-19]. Moreover, starting from bulk CuO reduction in hydrogen results either in Cu metal formation or in the intermediate formation of Cu_2O, depending on the hydrogen pressure [20]. Reducing CuO nanoparticles at 253 K in

CO has been reported to yield intermediate Cu_2O formation and metal was only detected after a prolonged reduction period [20]. The formation temperature of Cu_2O (460-510 K) and Cu (633-723 K) has also been reported to depend on the particle size [20]. Regarding the nickel oxide system, bulk reduction of NiO by hydrogen has been in the focus of a number of fundamental studies [7]. Reaction of NiO(100) single crystals with hydrogen under high-vacuum conditions occurs between 323 and 623 K after an induction period, whereas the reduction of bulk NiO or supported NiO/SiO_2 sets in only at very high temperatures (673-873 K) [7]. Conversely, the formation of nanoparticulate NiO is typically associated with the so-called Kirkendall effect, a process related to solid-state diffusional, interface-controlled processes, typically leading to porous core-shell structures [22-24].

Although obviously a wealth of information on many aspects of the formation and characterization of these particular oxides already exists, it should be noted that some information, with potential impact on the use of these oxides, is still missing. In the first place, this is related to the missing preparation of well-ordered, well-defined copper and nickel metal and oxide nanoparticles, combined with a study of formation and stability of the respective oxide nanoparticles under realistic pressures. Subsequently, the structural characterization of the transition from metal-to-oxide and oxide-to-metal by advanced electron microscopy techniques is extremely limited. A number of TEM-related studies exist [18,19,22-24], but either only on bulk samples [18,19] or, in the case of nanoparticles, typically only under (ultra) high vacuum conditions and/or on more irregular particles [22-24].

We therefore aim at providing a reproducible pathway to well-defined nanoparticulate copper and nickel systems and, subsequently, to elucidate the formation and stability limits of the associated nanoparticulate oxide systems. In this respect, an already well-established preparation routine following deposition of noble metal particles on vacuum-cleaved

NaCl(001) single crystalline substrates [25], acting as a structural mediator for the formation of well-defined and –ordered metal and oxide nanoparticles, will be exploited. Small particles of e.g. Pt, Rh, Pd, Re or Ir and PdO, In_2O_3 or Ga_2O_3 have been previously obtained [25-28], to name just a few. Due to the well-defined, epitaxial growth and the corresponding existence of low-indexed zone axes parallel to the electron beam, these model systems are especially well-suited for characterization by analytical high-resolution electron microscopy techniques.

2. Experimental

Thin Film preparation

The metal/metal oxide particles have been prepared via electron beam evaporation of copper (99.9999% purity Alfa Aesar) or nickel (99.98% purity, Alfa Aesar) onto a vacuum-cleaved NaCl (001) single crystal facet at a substrate temperature of 573 K in a dedicated high vacuum chamber (base pressure 10^{-6} mbar). The experimental conditions have been chosen in a way to result in nominal metal layer thicknesses of about 5 nm both for copper and nickel, resulting in particle sizes of 10-20 nm for copper and 10-30 nm for nickel. Subsequently, the Cu or Ni particles are embedded in a 25 nm thick layer of amorphous SiO_2, prepared by reactive deposition of SiO in a partial oxygen pressure of 10^{-4} mbar. The NaCl template is subsequently dissolved in water and the resulting thin film is transferred to a gold grid for electron microscopy. Routine inspection of the impurity level is carried out by energy-dispersive X-ray spectroscopy and basically revealed only peaks due to Cu, Ni, O or Si, with all other impurities typically well below the detection level. The purity of the substrate was ensured by freshly cleaving the NaCl(001) crystals immediately before deposition of the metal.

Oxidation and reduction

Thermal treatments in oxygen and hydrogen are carried out under flowing conditions of either 1 ml/s pure oxygen or pure hydrogen up to temperatures of about 873 K. After mounting the samples (i.e. the films on the gold grids) into the furnace, the temperature is ramped in 5 K/min to the desired temperature, followed by an isothermal period of 60 minutes. Finally, the samples are cooled down to room temperature in the respective gas atmosphere.

Electron Microscopy characterization

Structural characterization of the samples is carried out by two types of electron microscopes. Bright-field overview imaging and selected area electron diffraction (SAED) are carried out using a 100 keV Zeiss EM 10C microscope. Analytical high-resolution electron microscopy is performed using 200 kV FEI TECNAI F20 STWIN Analytical (Scanning-) Transmission Electron Microscopes (S)TEM equipped with a GATAN Tridiem energy filter. Prior to imaging, the samples were typically plasma-cleaned to remove surface carbon impurities. The SAED patterns were externally calibrated with respect to the Pd (111), (200) and (220) spots in a separately prepared thin film, investigated under identical conditions. Electron-energy loss spectra are background-corrected and corrected for plural scattering.

3. Results

3.1. Characterization of the as-grown states

3.1.1. The Cu-O system

Due to the amorphous nature of the SiO_2 support and the associated very low contrast, the particles can easily be identified as evenly distributed black and grey spots in Figure 1. In the present case, most of the particles exhibit rounded outlines and rarely, triangular-shaped, square or elongated particles are encountered. The contrast variations inside the particles are mainly due to Bragg contrast, that is, dark particles are in perfect Bragg orientation, while

grey ones are slightly tilted out of the perfect orientation for Bragg contrast. For further characterization, key structural film parameter such as the metal coverage, the particle density and the average particle diameter were determined. To measure the particle coverage, the tonal value of the image was set as to make visible all particles with equal contrast, subsequently the particles were masked (using the program Digital Micrograph©), counted, the respective area calculated and normalized to the area of the entire image. Using this method, a metal particle coverage of the support of ~ 30% was determined. The particle density amounted to $2.6 \cdot 10^{11}$ particles cm^{-2}, with an average diameter of ~ 12 nm (based on the analysis of 60 particles, measured along the longest diameter).

The corresponding SAED patterns (inset in Figure 1) reveal an almost perfect single-crystalline ordering of the particles, which is basically due to the perfect crystallographic matching of the face-centered Cu [29] and NaCl lattices [30], leading to epitaxial growth on the NaCl(001) crystal facet. Important spots of fcc Cu have been marked in black in the SAED pattern. However, a close inspection of the SAED pattern reveals the presence of a second phase, which has been identified as cubic Cu_2O (marked in white). The crystallographic analysis of both phases, alongside assignment of the spots to theoretical lattice planes of both structures, is shown in Table 1. For analysis, the powder diffraction data sets for Cu (face-centered cubic, lattice constant: 3.62 Å, space group: Fm-3m, pattern number 00-004-0836, [29]) and Cu_2O (cubic, lattice constant: 4.27 Å, space group: Pn-3m, pattern number 01-071-3645 [31]) have been used. It is worth noting, that Cu_2O exhibits single-crystalline ordering as well, with epitaxial relation both to Cu metal and NaCl. Hence, the epitaxial relations between Cu, Cu_2O and NaCl can be summarized as follws:

Cu [001] // NaCl[001], Cu_2O [001] // NaCl [001] and Cu_2O [001] // Cu [001]

The presence of Cu_2O is corroborated in the respective high-resolution images. Figure 2 shows such as representative image of a single Cu_2O particle, with a set of (200) lattice planes

running parallel to the particle edges (d_{exp}=2.14 Å, d_{theor} (200)=2.13Å [31]). The presence of both Cu metal and Cu_2O is also visible in the corresponding electron-energy loss spectra of the Cu L-edge (cf. Figure 7). Spectra, both characteristic for Cu metal and Cu_2O have been obtained on different areas of the sample. Spectrum b is typical for the presence of metallic Cu, with a suppressed white line at the L_3 edge at 931 eV [32]. In contrast, spectrum c shows a more distinct peak at the $L_{2,3}$ edge, clearly indicating the presence of copper in the valence state +I, i.e. Cu_2O [33].

3.1.2. The Ni-O system

Figure 3 C highlights an overview TEM image of the as-grown, initial Ni/SiO_2 catalyst. As in the case of Cu, the Ni particles are visible as black and grey spots. It appears, however, that the Ni particles exhibit a more defective nature, as they show more internal structure as the Cu counterparts. Bragg contrast is the dominant contrast mechanism also in this case. Particle coverage (20%), particle density ($3.7 \cdot 10^{11}$ particles cm^{-2}) are comparable to Cu, only the average particle diameter is somewhat higher at about 20-25 nm. In general, the Ni particles seem to exhibit more straight outlines and square, rectangular, rhombohedral or pentagonal outlines are frequently occurred. For determination of the three-dimensional morphology of the particles, dark-field images have been recorded and analyzed according to the method of Yacaman et al. [34]. In short, dark field images of small particles show distinct height contour lines, if the respective particle is not in perfect Bragg orientation and it exhibits a non-uniform particle thickness. From the arrangement of these contour lines, the angles of the limiting crystal planes of the particle can be determined and hence, its morphology [34]. Inset A shows such a dark-field image, taken with the Ni (200) spot, revealing that height contour lines are absent and hence, most of the particles do not exhibit a characteristic thickness variation or a corresponding morphology. We might therefore assume flattened particles and/or more irregular shapes. One notable exception is the square-like particle in the lower left corner

(encircled in inset A), which indeed shows two contour lines, indicating that the particle's morphology is a truncated half-octahedral. This evaluation is based on a comparison with previously deposited noble metal particles (such as Pt or Rh), where the half-octahedral morphology (among others) of the metal particles is much better pronounced [25,35].

The SAED pattern (inset B), reveals epitaxial growth of Ni on NaCl(001), as evidenced by its quasi single crystalline diffraction pattern. Some spots of the Ni structure (face-centered cubic, lattice constant: 3.50 Å, space group: Fm-3m, pattern number 00-001-1266 [36]) have been marked in black in the SAED pattern. As in the case of Cu, a second, oxidized species is also visible. This species is identified as NiO (face-centered cubic, lattice constant: 4.18 Å, space group: Fm-3m, pattern number 00-047-1049 [37]), which exhibits a similarly well-ordered pattern (marked in black). Hence, epitaxial growth of fcc Ni and fcc NiO on fcc NaCl mainly occurs in the relations:

Ni [001] // NaCl[001], NiO [001] // NaCl [001] and NiO [001] // Ni [001]

For both Ni and NiO particles, the dominant zone axis is [001] with respect to the electron beam. An assignment of the experimentally determined lattice spacings to those of the Ni and NiO structures is provided in Table 2. Figure 4 shows an example of a high-resolution image of a single square-like Ni particle with two sets of perpendicular (200) lattice planes running along the particle edges. NiO particles are similarly encountered in HRTEM images (not shown).

In addition, evidence about the presence of both Ni and NiO is again provided by electron energy loss spectroscopy (cf. Figure 8). Spectra b and c of the Ni L-edge are typical for metallic and oxidic Ni, respectively. The determination of the oxidation state is based on a comparison of the white line ratio Ni $L_{2,3}$ edge [32]. In the case of metallic Ni, the relative

intensities of L_3 (at 850 eV) to L_2 (at 870 eV) are close to 1.5-1.8 (see spectrum b), whereas for NiO, this ratio increases to 2.2-2.5 (see spectrum c).

3.1.3. Comparative Discussion

For a better understanding of the structural, compositional and morphological details of the Cu- and Ni composite particles, the above-discussed findings are put into perspective to other, similarly deposited (noble) metal particles. From a structural and growth perspective kind of view, only marginal differences to the previously studied Pt, Rh, Pd, Ir and Re metal particles are noticeable [35]. Epitaxial growth on NaCl(001) cleavage faces has been observed for all studied metal systems [35], and both Cu and Ni are no exception to that rule. The dominating zone axis is [001], to a lesser extent [011], and a high degree of azimuthal ordering is usually observed upon deposition at elevated temperature $T \geq 573$ K. Hence, a cube/cube orientational relationship between metal/oxide and NaCl is almost exclusively observed. Particle densities, particle coverage and average particle diameters are comparable to Pt, Rh and Pd, where under similar experimental conditions particle densities between $3.5 \cdot 10^{11}$ and $1.2 \cdot 10^{11}$ particles cm^{-2} (between 573 and 623 K deposition temperature), particle coverages between 10 and 25% and average particle diameters in the range of 5-15 nm (for Pt, Rh and Pd at lower nominal metal thicknesses) have been observed [35]. Particle morphologies, however, vary. Whereas the morphology of Pt particles can be described as basically truncated half-octhaedral (with limiting (001) and {111} planes) and of Rh by the presence of many different morphologies such as half-octhadral, dodecahedral or pseudo-pentagonal [35], Cu appears to be more related to Pd. The latter two appear generally more rounded, due to the presence of {110} or high-indexed facets [35]. Hence, in the present case, for Cu distinct particle morphologies with varying particle thicknesses (such as octhedral in the case of Pt) are mostly absent. For Ni metal particles, in some cases distinct two-dimensionally projected

particle morphologies can be observed in the bright field images, as it has been the case for Rh: these include rectangular, pentagonal and truncated rhomobohedral particles (see markers a, b and c in Figure 3 C). By comparison of the dark-field images with those of Pt or Rh [35], the rectangular, square-like particles are associated with a truncated half-octhadral morphology.

3.2. Formation of the oxide phases

3.2.1. The Cu-O system

The oxidation of the small Cu/Cu_2O particles to possibly CuO was followed by TEM imaging, selected area electron diffraction and electron-energy loss spectroscopy. The latter spectra show beginning formation of a CuO phase already at 473 K (spectrum d in Figure 7). A ahoulder, developing at 935 eV and 953 eV at the Cu L_3 and L_2 edges are clearly visible and indicates the formation of Cu valence state +II. However, Cu +I appears to still be the dominating valence state, as its Cu L_3 peak is still very pronounced [32,33]. Figure 5 A shows that although the oxidation temperature is increased to 673 K the overall structural features of the Cu/Cu_2O particles are not altered: strong sintering is not observed and the particle diameter still is around 10-15 nm. Particle density and metal coverage both appear unaffected by the treatment. The SAED pattern (inset in Figure 5A), however, reveals a distinct change in the composition of the particles. Careful analysis of the pattern shows the presence of a single, well-ordered base-centered monoclinic CuO phase (lattice constant: a=4.68 Å, b=3.42 Å, c=5.13 Å, β=99.51°; space group: C2/c, pattern number 00-048-1548 [38]). The almost single-crystalline pattern indicates epitaxial or at least well-ordered growth of CuO on Cu_2O. Further raising the oxidation temperature to 873 K does not change the composition of the oxide phase and still, only CuO is observed (cf. SAED inset in Figure 5 B). The corresponding EEL spectra correspondingly show only CuO and the peak of Cu_2O is clearly absent. In contrast, at 873 K, the film morphology has substantially altered.

As shown in Figure 5 B, the average particle diameter has increased to about 20 nm and the particle outlines significantly sharpened. Mostly irregular outlines, but sometimes pentagonal or hexagonal shapes are observed. Such particle reconstructions are known to occur by exposure to a specific gas atmosphere at elevated temperatures (e.g. drop-like-to-cubic Pt particles upon exposure to hydrogen at 900 K or hydrogen sulphide at 673 K [39,40], shape variations of Pd particles due to oxygen adsorption under UHV conditions [41]), thereby stabilizing specific crystal facets over others due to variation of the surface free energy and the associated energy gain. The behavior of the CuO particles at 873 K (which is well below the melting point of CuO, being 1599 K [6]), however, indicates that at these temperatures the atomic diffusion on the surfaces is already high enough for these particle sizes (20-30 nm) to reach the equilibrium crystal morphology. Figure 6 finally highlights a high-resolution TEM image of a CuO particle with possible (111) and (11-1) lattice fringes ((d_{exp}=2.50 Å, d_{theor} (11-1) = 2.52Å, d_{exp}=2.31 Å, d_{theor} (111)=2.32Å [38]), possibly formed via coalescence of two individual CuO particles.

3.2.2. The Ni-O system

The oxidation of small Ni/NiO particles in principle composition-wise follows a similar trend as for Cu. As indicated by Figure 8, the EEL spectrum d, measured after oxidation at 473 K, is typical for NiO, as deduced from the relative intensity ratio of 2.5:2 Ni L_3 to L_2 peak. Even after oxidation at 673 K (spectrum e), the spectral features do not change. In contrast, the TEM images taken after oxidation at temperatures $T \geq 473$ K reveal significant structural differences to Cu. Mapping mass thicknesses we used high angle annular darkfield (HAADF) STEM. In this experimental set-up, Rutherford scattered electrons are used for imaging, the intensity being dependent on the atomic number Z. HAADF images after oxidation at 473 K show an array of rounded grains of 20-30 nm in size with clearly visibile protrusions in the center (Figure 9). This is an effect which is already well-documented for a number of oxide

particles including CoO, FeO, Al_2O_3, ZnO, Cu_2O or also NiO and usually termed the (nanoscale) Kirkendall effect [22,42]. The driving force are diffusivity differences at inorganic interfaces, which lead to hollow aggregates with binary compositions of metal and corresponding oxide [22]. In principle, due to pronounced differences in the average number Z, the hollow structures are much better seen in HAADF than in conventional TEM images. The SAED pattern (inset in Figure 9) reveals that despite substantial structural re-arrangements, NiO and Ni both remain practically epitaxially-ordered. Figure 10 in turn shows two single hollow-sphered particles with de-centered voids and atomically-resolved Ni (200) lattice fringes (d_{exp}=2.08 Å, d_{theor} (200)=2.09 Å [37]) see also the FFT pattern as inset in Figure 10 B). We emphasize already at this point, that - due to the exploitation of a single-crystalline NaCl(001) substrate - for the first time epitaxially grown NiO hollow spheres could be obtained.

3.2.3. Stability of the oxide phases

Despite many studies on the formation of the Cu_2O/CuO and NiO phases, comparably little attention has been given to investigating their stability. For nano-particulate systems, the information is scarce [24], for well-defined systems virtually non-existent. As for many applications, the stability under reducing conditions is imperative, we finally aimed at a comparison of the stability of CuO and NiO upon treatment in hydrogen, in order to correlate our measurements to literature-reported data [24]. Figure 11 therefore highlights a comparison between Cu/C_2O (A) and Ni/NiO (B) particles, after an identical treatment of oxidation in oxygen at 673 K, followed by reduction in hydrogen at 673 K. Substantial differences are easily recognizable: whereas the former CuO particles (formed after oxidation at 673 K) are transformed into very irregular particles with a pronounced shell and are more irregular periphery consisting of several small grains, the NiO particles (formed after oxidation at 673 K) almost entirely lose their porous structure and uniform, homogeneous particles are

obtained. In the latter case, sintering is pronounced. Composition-wise, the SAED patterns are generally weak in contrast and for the Cu case reveal a mixture of CuO, Cu_2O and Cu (see Table 1). This is corroborated by the corresponding EEL spectra, which (cf. Figure 7, spectrum a) clearly show a shift from Cu +II to Cu +I. In fact, the EEL spectra exhibit the same shape as before the oxidation process. The same trend has been observed for reduction of NiO. EEL spectra indicate the presence of Ni in lower valence states than +II, as deduced from the reversal of the intensity ratio of the Ni L_3 and L_2 peaks back to almost 1:1 (cf. Figure 8, spectrum a). The SAED pattern (inset in Figure 11 B) cannot be explained by the simple presence of NiO, Ni metal or any other oxygen-containing Ni species. Rather, reduction of NiO led to the formation of a nickel silicide species, specifically, Ni_3Si_2. An assignment of the experimentally determined lattice spacings to the base-centered orthorhombic Ni_3Si_2 structure (a=12.22Å, b=10.80Å, c=6.92Å, space group Cmc21, pattern number 00-017-0881 [42]) is shown in Table 2. Representative HRTEM images of both Cu and Ni samples are shown in Figure 12. Figure 12 A shows an ruptured CuO particle, whose outer peripheries show atomically resolved lattice spacings of differently oriented micrograins of remaining CuO, exhibiting (111) lattice fringes (d_{exp}=2.30 Å, d_{theor} (111)=2.32Å). In contrast, Figure 12 B shows a high-resolution electron micrograph of a single Ni_3Si_2 particle with a set of lattice spacings, several of which have been marked by circles in the Fast Fourier Transfrom pattern shown as inset.

3.2.4. Comparative Discussion

To put the results into perspective of literature-reported data, as well as to highlight the novelty of this work, we will divide the comparative discussion into three main parts: (i) discussion of the similarities and differences of oxide formation between our and other works on Cu and Ni, including comparison of bulk and nanoparticulate systems, (ii) discussion of the formation and stability of hollow spheres in the Cu and Ni systems and (iii) a discussion

of oxide formation and stability of nanparticulate Cu and Ni to oxidation of other metals, specifically Rh and Pd.

For easier correlation of the oxidation and stability of Cu/Cu_2O nanoparticles to literature-reported data, Table 3 highlights a compact overview of important observations on different Cu systems during formation of the different oxide phases. These data hence include both bulk and nanoparticulate systems as well as preparation by oxidation of Cu metal (for Cu_2O and CuO) and reduction of CuO (for Cu_2O). It is important to note that this list is far from being complete, as in literature especially the oxidation of bulk Cu is already scrutinized from almost all points of view [1,2,11,17-21]. Special attention has been paid to the early stages of Cu oxidation as to follow the transition from Cu to Cu_2O and CuO [17-21,43-45]. Table 3 therefore rather presents an overview of systems which can be conveniently compared to our results. Oxidation of Cu nanoparticles to Cu_2O has been studied by Tokozakura et al., who observed core-shell Cu_2O particles after oxidation in air at 323-373 K [46]. Reductively, Cu_2O has also been prepared by Pike et al., who observed the sequence $CuO \rightarrow Cu_2O \rightarrow Cu$ after treating CuO in flowing CO between 513 and 723 K [20]. Similarly, bulk samples of Cu or CuO have been exploited to study the transition to Cu_2O [18,19,47]. Yang and Zhou et al. exploited in-situ TEM to study the Cu_2O formation from bulk Cu samples under UHV conditions and observed Cu_2O over a wide range of temperatures between 423 and 1273 K. No CuO has been obtained [18,19]. Matyas observed CuO formation starting from bulk Cu metal between 573 and 1303 K, with intermediate Cu_2O [17]. Conversely, Rodriguez et al. either observed direct transition from bulk CuO to Cu metal or a sequence $CuO \rightarrow Cu_2O \rightarrow Cu$, depending on the reaction conditions upon reduction in hydrogen [47]. However, using both hydrogen or CO as reduction agent, a direct transition without intermediate Cu_2O formation could be observed [20,47]. From our results it is clear, that well-defined CuO nanoparticles, possibly adopting their thermodynamic equilibrium morphology could easily be obtained by

oxidation in oxygen at and above 473 K. However, structure-and phase pure Cu_2O could not be obtained using this routine. It is important to note, that due to the pyrophoric nature of small Cu particles [6], phase-pure Cu metal nanoparticles are impossible to prepare without post-reductive treatments. Following the reductive pathway from CuO nanoparticles to Cu metal particles in hydrogen, a sequential reaction is found to be prevalent, which is accompanied by a substantial rupture of the CuO particle morphology, leaving a mixture of Cu metal, Cu_2O and CuO behind. Correlation to other nanoparticulate CuO systems is not straightforward, since data only exist for CO as a reduction agent under in-situ conditions [20]. After reduction at 673 K, Cu metal is present both in our work (using hydrogen) and in the work of Pike et al. (using CO [20]). Regarding Ni nanoparticulate systems, a wealth of literature is obtainable for all kinds of different methods for the fabrication of especially Ni/NiO core-shell particles [48,49]. However, no detailed study on the oxidation and stability of Ni nanoparticles has been performed. Some data are available for the reduction of NiO powders in hydrogen [7], which show beginning reduction of NiO at temperatures between 523-623 K [7], which is apparently in good agreement with the data presented here, showing full decomposition of NiO to Ni metal at 673 K (as a precursor to silicide formation).

Since the literature about the formation of hollow-nanospheres is far to exhaustive to be discussed in detail here, we restrict ourselves to the discussion of the Cu and Ni case [22-24] . Formation of hollow NiO structures starting from differently sized, round, ligand-stabilized Ni nanoparticles (10-100 nm) at temperatures between 473-773 K, Ni nanoparticles between 573-673 K or Ni nanowires in similar temperature regions has recently been observed and explained by the different diffusion kinetics of Ni and O [22] . However, no attention has been given to the investigation of either well-shaped Ni nanoparticles or the stability of the hollow structures in general. Regarding the former, no substantial influence of the particle morphology on the formation of the hollow structures can be deduced from our results. The

onset temperature of formation of the hollow nanostructure is quite comparable to other systems [22-24]. Of crucial importance of the thorough understanding of the Kirkendall effect obviously also is the determination of the stability limits of the hollow nanostructures. This is a question which rarely has been addressed in detail experimentally [46], but recent theoretical work highlights the inherent thermodynamical instability of the hollow structures [50]. It is shown that due the equilibration of the chemical potential differences between inner and outer surfaces of the hollow spheres annealing leads to the annihilation of the void and that this processes occurs on the timescale between seconds and minutes at 500-673 K, depending on surface energy, diffusitivity and size of the structures. This has been calculated for Au [50] and shown experimentally for bimetallic Cu_3Sn voids accompanied by formation of a Sn-richer bimetallic [51]. Our results suggest, that at temperatures of 673 K the diffusion of Ni atoms to the inner surface is already high enough to finally lead to the annihilation of the void within 60 minutes. Nakamura reported the beginning shrinkage of larger hollow NiO particles under high vacuum conditions ($5 \cdot 10^{-7}$ mbar) to Ni metal at 623 K [22]. Regarding Cu, the situation appears to be more complex due to the discrepancy as to whether the voids form or not accompanying oxidation of small Cu particles. Nakamura et al. report in a number of papers the formation of Cu_2O hollow nanostructures upon oxidation of Cu particles with an average size of ~ 25 nm in air between 323 and 373 K for 6-20 minutes [22, 46]. Also in this case, a size-dependent Kirkendall effect is reported. This results are in obvious contrast to the ones reported here, which under no experimental conditions show formation of hollow nanostructures for either Cu_2O (or CuO). Two possible explanations are in principle at hand, including a Cu particle size effect and a possible influence of the oxidation time/temperature. Nakamura report that the growth of the Cu_2O oxide layer on smaller nanoparticles is generally more suppressed relative to larger ones [46]. As our Cu particles definitely exhibit a smaller average size (~ 10 nm) we might therefore anticipate suppressed formation of hollow Cu_2O nanostructures. Secondly, our oxidation temperatures and times are generally higher than

applied by Nakamura (473-873 K; 60 minutes [46]), potentially favoring the formation of a bulk oxide phase.

Correlating the oxidation behavior of Cu and Ni nanoparticles to other comparable systems, the question on the formation mechanism of the oxide phases arises. Specifically, we might either anticipate three-dimensional bulk oxide growth or formation of a core-shell-type oxide phase, both of which have been observed for several systems, e.g. Rh and Pd [35,52]. A representative of the former is PdO, which has been shown to follow epitaxial bulk oxide growth on small Pd particles at 573-673 K [52]. In contrast, Rh particles have been observed to be covered by a thin skin of Rh_2O_3 at comparable temperatures due to favoured wetting of Rh and Rh_2O_3 at the metal-oxide interface [35]. On the basis of our results and a comparison to literature-reported data it is clear, that in the early stages of Ni oxidation to NiO a core-shell structure is present. For Cu, ambivalent results are obtained: whereas our results suggest that oxidation of Cu to Cu_2O (and especially to CuO) primarily follows three-dimensional growth, Nakamura reports similar (hollow) core-shell structures as in the case of NiO or Rh_2O_3 [46]. These findings suggest that the formation mechanism of the oxide is size- and condition-dependent.

4. Conclusions

In conclusion, the NaCl(001) growth template has once again shown its capabilities in the growth of Cu/Cu_2O and Ni/NiO nanoparticles with defined structure and morphology. This is an obvious advantage over other reported systems and allows not only the detailed investigation of the structure and morphology of the as-grown states, but in turn also allows the in-depth characterization of phase transformations depending on experimental conditions, such as reaction temperature or gas atmosphere. This has for Cu and Ni particles been successfully exemplified for the interaction with oxygen, but can be deliberately extended to other interactions, e.g. with hydrogen to study the reductive formation of bimetallic phases for

oxide-supported metal nanoparticles. The information that can be gained from the use of these systems is not restricted to rather simple gas-solid interactions but can e.g. be extended to the studies of full catalytic reactions with the possible aim to establish structure-activity/selectivity relationships. This is greatly facilitated by the use of the well-defined nanoparticulate systems, as presented above.

5. Acknowledgements

This work was financially supported by the Austrian Science Fund (FWF) through grant F4503-N16 and has been performed within the framework of the Forschungsplattform Materials- and Nanoscience.

Tables

Table 1: Correlation of the experimentally determined lattice spacings $d(hkl)_{exp}$ [Å] on Cu/SiO_2 after different thermal treatments to those of the face-centered cubic Cu [29], cubic Cu_2O [31] and base-centered monoclinic CuO structures [38] ($d(hkl)_{theor}$ [Å]), alongside assignment to distinct theoretical lattice planes, characterized by $d(hkl)_{theor}$.

Cu/SiO_2 as grown			**Cu/SiO_2 O673**			**Cu/SiO_2 O673/H673**		
Assignment			**Assignment**			**Assignment**		
d $(hkl)_{exp}$	**Lattice plane**	**d $(hkl)_{theor}$**	**d $(hkl)_{exp}$**	**Lattice plane**	**d $(hkl)_{theor}$**	**d $(hkl)_{exp}$**	**Lattice plane**	**d $(hkl)_{theor}$**
3.03	Cu_2O (110)	3.02	2.77	CuO (110)	2.75	2.47	Cu_2O (111)	2.46
2.14	Cu_2O (200)	2.13	2.53	CuO (11-1)/ CuO (002)	2.53	2.30	CuO (111)	2.32
1.85	Cu (200)	1.81	2.31	CuO (111)/ CuO (200)	2.33	2.14	Cu_2O (200)	2.13
1.52	Cu_2O (220)	1.51	1.85	CuO (20-2)	1.86	2.05	Cu (311)	2.08
1.31	Cu (220)	1.28	1.59	CuO (202)	1.58	1.29	Cu_2O (311)	1.28
							Cu (220)	1.28

Table 2: Correlation of the experimentally determined lattice spacings $d(hkl)_{exp}$ [Å] on Ni/SiO_2 after different thermal treatments to those of the face-centered cubic Ni [36] and face-centered cubic NiO [37] and base-centered orthorhombic Ni_3Si_2 structures [42] ($d(hkl)_{theor}$ [Å]), alongside assignment to distinct theoretical lattice planes, characterized by $d(hkl)_{theor}$.

Ni/SiO_2 as grown			**Ni/SiO_2 O473**			**Ni/SiO_2 O673/H673**		
Assignment			**Assignment**			**Assignment**		
$d(hkl)_{exp}$	**Lattice plane**	**$d(hkl)_{theor}$**	**$d(hkl)_{exp}$**	**Lattice plane**	**$d(hkl)_{theor}$**	**$d(hkl)_{exp}$**	**Lattice plane**	**$d(hkl)_{theor}$**
2.13	NiO (200)	2.09	2.41	NiO (111)	2.41	3.31	Ni_3Si_2 (311)	3.34
2.09	Ni (111)	2.04	2.08	NiO (200)	2.09	2.09	Ni_3Si_2 (150)/ Ni_3Si_2 (023)	2.12/2.12
1.81	Ni (200)	1.77	1.47	NiO (220)	1.48	2.04	Ni_3Si_2 (600)	2.03
1.51	NiO (220)	1.48	1.26	NiO (311)	1.26	2.00	Ni_3Si_2 (242)	2.01
1.27	Ni (220) NiO (311)	1.25 1.26	1.19	NiO (222)	1.21	1.93	Ni_3Si_2 (512)/ Ni_3Si_2 (531)	1.96/1.94
						1.82	Ni_3Si_2 (621)	1.83
						1.74	Ni_3Si_2 (532)/ Ni_3Si_2 (004)	1.73/1.74

Table 3: Overview of important formation and decomposition conditions for representative bulk and nanoparticle Cu, Cu_2O and CuO systems, as described in the literature.

System	**Phase**			**treatment pressure**	**Particle size**
	Cu_2O	*CuO*	*Cu*		
bulk[17]	176 to 523 K	573-1303 K	Initial state	200 mbar O_2	
bulk[18, 19]	423-1273 K	-	Initial state	$6 \cdot 10^{-4}$ mbar O_2	
bulk[47]	-	Initial state	423-573 K	1 ml/min H_2	
bulk[47]	483, 543, 573 K	Initial state	483, 543, 573 K	$5 \cdot 10^{-2}$ ml/min H_2	
nanoparticles [20]	513-463 K	Initial state	723-633 K	1 ml/min CO	5-12 nm
nanoparticles[20]	523 K	Initial state	after 45 min	1 ml/min CO	11 nm
nanoparticles [46]	323-373 K	-	Initial state	1000 mbar air	23.5 nm

Figure Captions

Figure 1: Overview bright-field TEM image of small Cu/Cu_2O particles embedded in a matrix of amorphous SiO_2. The inset highlights the SAED pattern, with marked spots of the Cu structure (black) and the Cu_2O structure (white).

Figure 2: Atomically resolved image of a single square-shaped Cu_2O particle with (200) lattice spacings running parallel to the particle edges. The inset shows the Fast Fourier Transform, with marked (200) and (-200) spots.

Figure 3: Overview bright-field TEM image of small Ni/NiO particles embedded in a matrix of amorphous SiO_2 (panel C). Panel A highlights the dark-field image of a representative sample region with an array of Ni/NiO particles, panel B the corresponding SAED pattern.

Figure 4: Atomically resolved image of a single square-shaped Ni particle with two sets of perpendicular (200) lattice spacings running parallel to the particle edges. The inset shows the Fast Fourier Transform, with marked {200} spots.

Figure 5: Overview bright-field TEM images of small CuO particles, obtained after oxidation of the particles shown in Figure 1 at 673 K (panel A) and 873 K (panel B). The insets highlight the respective SAED pattern.

Figure 6: Atomically resolved image of a CuO particle with {111} lattice spacings, along with its Fast Fourier Transform pattern.

Figure 7: Set of electron-energy loss spectra obtained after different treatments of the Cu/Cu_2O particles. a) after oxidation at 673 K followed by reduction at 673 K, b) as-grown,

Cu particle, c) as-grown Cu_2O particle, d) after oxidation at 473 K, e) after oxidation at 673 K, f) after oxidation at 873 K.

Figure 8: Set of electron-energy loss spectra obtained after different treatments of the Ni/NiO particles. a) after oxidation at 673 K followed by reduction at 673 K, b) as-grown, Ni particle, c) as-grown NiO particle, d) after oxidation at 473 K, e) after oxidation at 673 K.

Figure 9: High-angle annular dark field image of small Ni/NiO particles after oxidation at 473 K. The inset shows the corresponding SAED pattern with marked Ni (grey) and NiO spots (black).

Figure 10: Atomically resolved images of hollow Ni/NiO particles with (200) lattice spacings. The inset in B highlights the Fast Fourier Transform, with two sets of marked perpendicular {200} spots.

Figure 11: Overview bright-field TEM images of CuO particles (panel A) and NiO particles (panel B) after reduction at 673 K in hydrogen. The insets shows the corresponding SAED patterns.

Figure 12: Atomically resolved images of Cu/Cu_2O (panel A) and Ni/NiO (panel B) particles after oxidation at 673 K followed by reduction in hydrogen at 673 K. The insets show the corresponding Fast Fourier Transform patterns. As a guidance, some spots have been indexed.

References

[1] Model Systems in Catalysis: Single Crystals to Supported Enzyme Mimics (R. Rioux, Ed.), Springer, New York, 2010

[2] Synthesis, Properties and Applications of Oxide Nanomaterials, J. A. Rodriguez, Wiley, Weinheim, 2007

[3] B. Delmon in Handbook of Heterogeneous Catalysis (G. Ertl, H. Knözinger, J. Weitkamp, Eds.), Wiley, Weinheim, 1997, pp. 264-277

[4] Transition Metal Oxides: Surface Chemistry and Catalysis, H. H. Kung, Elsevier, Amsterdam, 1989

[5] X. Wang, J. C. Hanson, A. I. Frenkel, J.-Y. Kim, J. A. Rodriguez, J. Phys. Chem. B 108 (2004) 13667

[6] Lehrbuch der Anorganischen Chemie, A. F. Hollemann, E. Wiberg, Walter de Gruyter, 102. Auflage, Berlin

[7] J. A. Rodriguez, J. C. Hanson, A. I. Frenkel, A.-Y. Kim, M. Perez, J. Amer. Chem. Soc. 124 (2002) 346 and references therein

[8] K.A. Hofmann, Berichte der deutschen chemischen Gesellschaft 51 (1918) 1334

[9] G.G. Jernigan, G.A. Somorjai, J. Catal. 147 (1994) 567

[10] M. Moreno, L. Bergamini, G.T. Baronetti, M.A. Laborde, F.J. Mariño, International Journal of Hydrogen Energy 35 (2010) 5918

[11] J. B. Wang, D. Tsai, T.-J. Huang, J. Catal. 208 (2002) 370

[12] F. Fischer, H. Tropsch, Brennst.-Chem. 9 (1928) 39

[13] M. Garcia-Dieguez, I.S. Pieta, M.C. Herrera, M.A. Larrubia, L.J. Alemany, J. Catal. 270 (2010) 136

[14] M. Tada, S. Zhang, S. Malwadkar, N. Ishiguro, J.-I. Soga, Y. Nagai, K. Tezuka, H. Imoto, S. Otsuka-Yao-Matsuo, S.-I. Ohkoshi, Y. Iwasawa, Angew. Chemie Intl. Ed. 51 (2012) 9361

[15] H. Takano, K. Izumiya, N. Kumagai, K. Hashimoto, Appl. Surf. Sci. 257 (2011) 8171

[16] Z. Wang, W. Wang, G. Lu, International Journal of Hydrogen Energy 28 (2003) 151

[17] M. Matyas, Czech. J. Phys. 5 (1955) 214

[18] J.C. Yang, M.D. Bharadwaj, G. Zhou, L. Tropia, Microsc. Microanal. 7 (2001) 486

[19] G. Zhou, J.C. Yang, Appl. Surf. Sci. 210 (2003) 165-170.

[20] J. Pike, S.-W. Chan, F. Zhang, X. Wang, J. Hanson, Appl. Catal., A 303 (2006) 273

[21] J.A. Rodriguez, J.Y. Kim, J.C. Hanson, M. Perez, A.I. Frenkel, Catal. Lett. 85 (2003) 247

[22] J. G. Railsback, A. C. Johnston-Peck, J. Wang, J. B. Tracy, ACS Nano 4 (2010) 1913 and references therein

[23] R. Nakamura, D. Tokozakura, H. Nakajima, J. G. Lee, H. Mori, J. Appl. Phys. 101 (2007) 074303

[24] R. Nakamura, H. Nakajima, H. Mori, Diffusion and Defect Data-Solid State Data, Pt. A: Defect and Diffusion Forum 289-292 (2009) 673

[25] G. Rupprechter, K. Hayek, H. Hofmeister, J. Catal. 173 (1998) 409

[26] D. Wang, S. Penner, D.S. Su, G. Rupprechter, K. Hayek and R. Schlögl J. Catal. 219 (2) (2003) 434

[27] H. Lorenz, M. Stöger-Pollach, S. Schwarz, J. Bernardi, Ch. Pfaller, B. Klötzer, S. Penner, J. Phys. Chem. C 112 (2008) 918

[28] S. Penner, B. Jenewein, H. Gabasch, B. Klötzer, D. Wang, A. Knop-Gericke, R. Schlögl, K. Hayek, J. Chem. Phys. 125 (2006) 094703

[29] T. Swanson, Natl. Bur. Stand. (U.S.), Circ. 539, I (1953) 15

[30]

[31] A. Kirfel, K. D. Eichhorn, Acta Crystallogr. A 46 (1990) 271

[32] C. C. Ahn, O. Krivanek, EELS Atlas, Gatan ©, 1983

[33] J. P. Ngantcha, M. Gerland, Y. Kihn, A. Riviere, Eur. J. Appl. Phys. 29 (2005) 83

[34] M. Jose Yacaman, L. D. Romeu, A. Gomez, Z. A. Munir, IFUNAM (1980) 3

[35] G. Rupprechter, K. Hayek, L. Rendon, M. Jose Yacaman, Thin Solid films 260 (1995) 148

[36] T. Swanson, Natl. Bur. Stand. (U.S.), Circ. 539, I (1953) 13

[37] K. Martin, G. McCarthy, north Dakota State Univ., Fargo, ND, USA, ICDD Grant-in-Aid (1991)

[38] J. Langford, D. Louer, J. Appl. Crystall. 24 (1991) 149

[39] A. C. Shi, R. I. Masel, J. Catal. 120 (1989) 421

[40] P. J. F. Harris, Surf. Sci. 185 (1087) L459

[41] H. Graoui, S. Giorgio, C. R. Henry, Surf. Sci. 417 (1998) 350

[42] Y. D. Yin, R. M. Rioux, C. K. Erdonnez, S. Hughes, G. A. Somorjai, A. P. Alivisatos, Science 304 (2004) 711

[42] G. Pilstrom, Acta Cham. Scand. 15 (1961) 893

[43] J. Cunningham, G.H. Al-Sayyed, J.A. Cronin, C. Healy, W. Hirschwald, Appl. Catal. 25 (1986) 129-138

[44] R. Guan, H. Hashimoto, T. Yoshida, Acta Cryst. B B40(2) (1985) 109

[45] J. C. Yang, D. Evan, L. Tropia, Appl. Phys. Lett. 81 (2002) 241

[46] D. Tokozakura, R. Nakamura, H. Nakajima, J. G. Lee, H. Mori, J. Mater. Res. 22 (2007) 2930

[47] J. Y. Kim, J. A. Rodriguez, J. C. Hanson, A. I. Frenkel, P.l. Lee, J. Am. Chem. Soc. 125 (2003) 10684

[48] C. L. Luan, J. Phys. Chem. C 114 (2010) 2124 and references therein

[49] N. Cordente, B. Toustou, V. Colliere, C. Amiens, B. Chaudret, M. Verelst, M. Respaud, J. Broto, Compte Rendues de l'Academie des Sciences, Serie IIc 4 (2001) 143 and references therein

[50] K. N. Tu, U. Gösele, Appl. Phys. Lett. 86 (2005) 093111

[51] C. Y. Liu, K. N. Tu, T. T. Sheng, C. H. Tung, D. R. Frear, P. Elenius, J. Appl. Phys. 87 (2000) 750

[52] S. Penner, B. Jenewein, H. Gabasch, B. Klötzer, D. Wang, A. Knop-Gericke, R. Schlögl, K. Hayek, J. Chem. Phys. 125 (2006) 094703

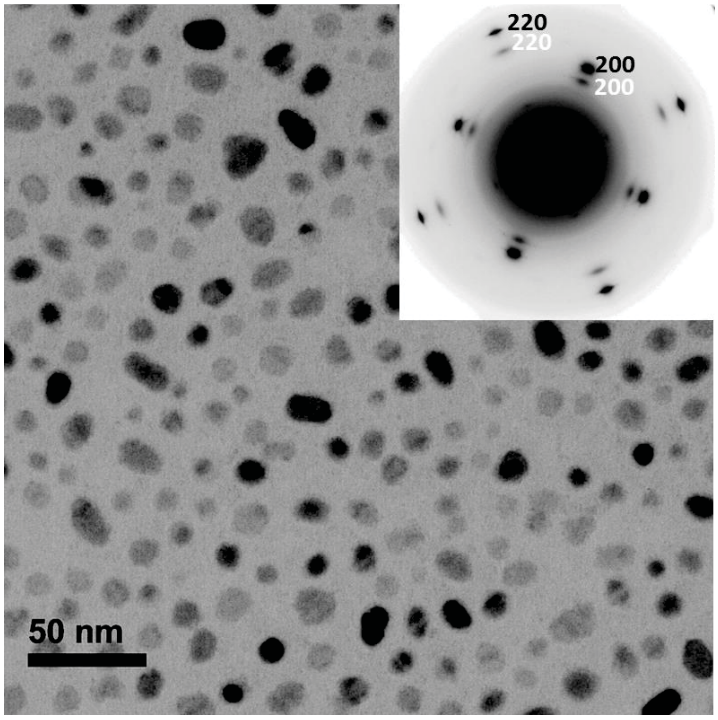

Figure 1

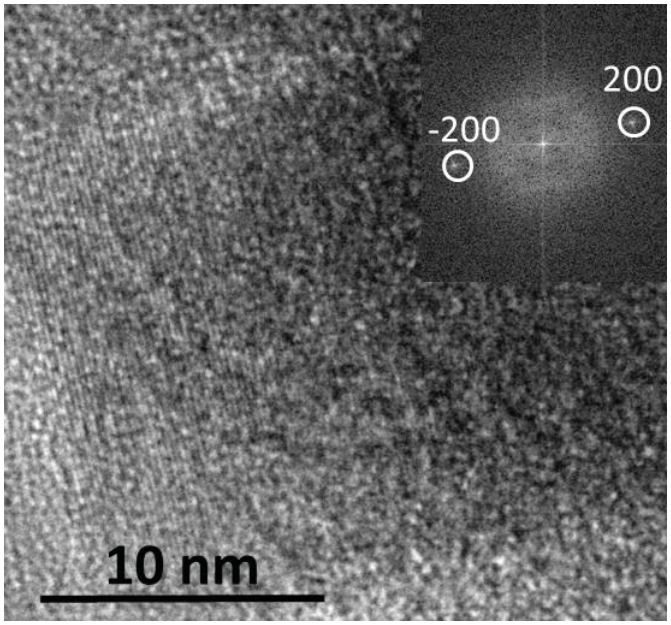

Figure 2

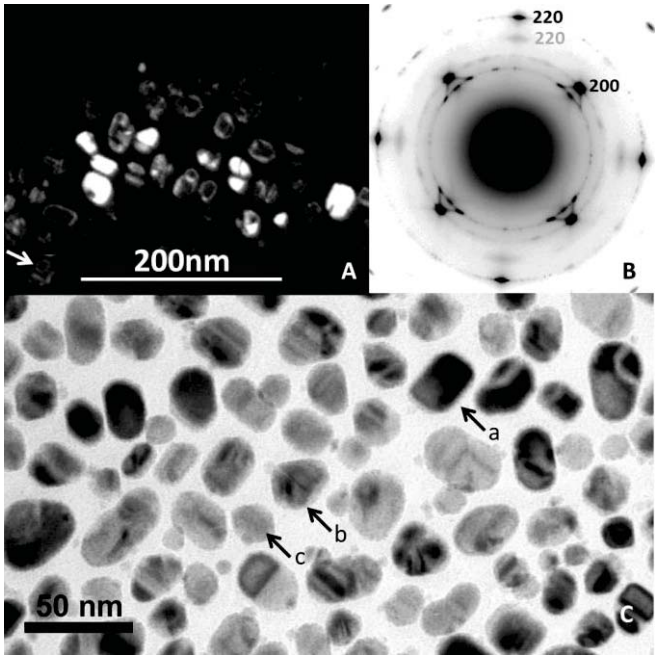

Figure 3

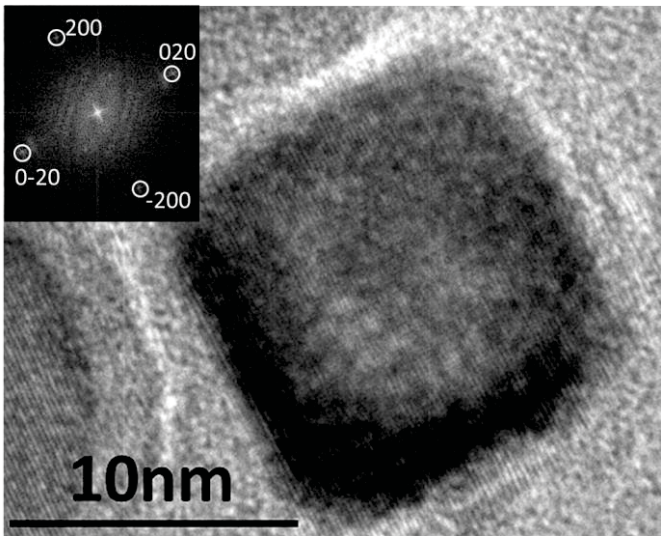

Figure 4

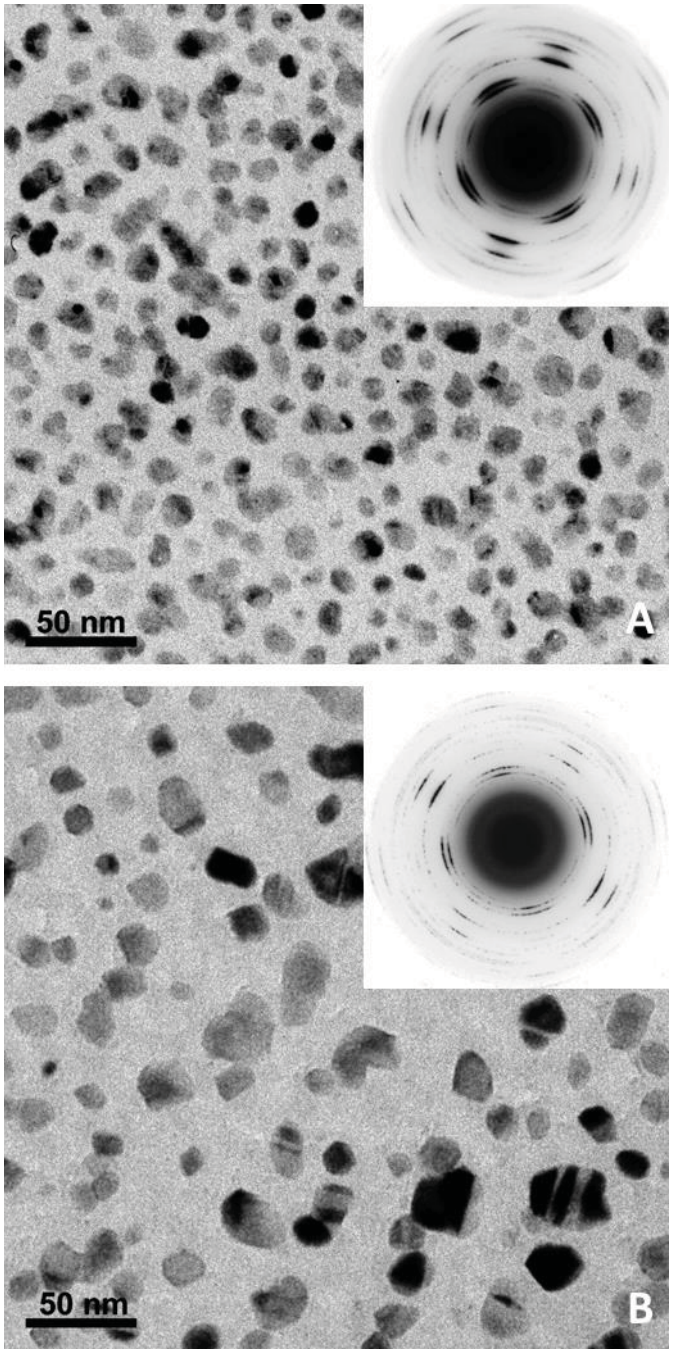

Figure 5

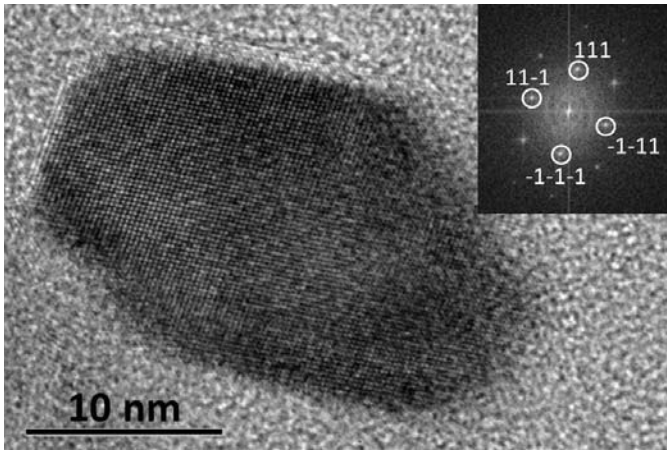

Figure 6

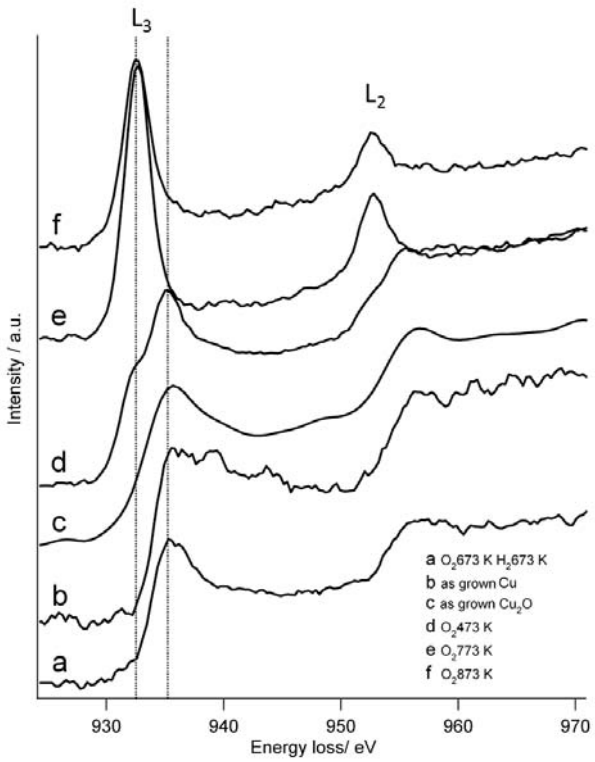
L3
L2
f
e
d
c
b
a
Intensity / a.u.
930
940
950
960
970
Energy loss/ eV
a O2673 K H2673 K
b as grown Cu
c as grown Cu2O
d O2473 K
e O2773 K
f O2873 K

Figure 7

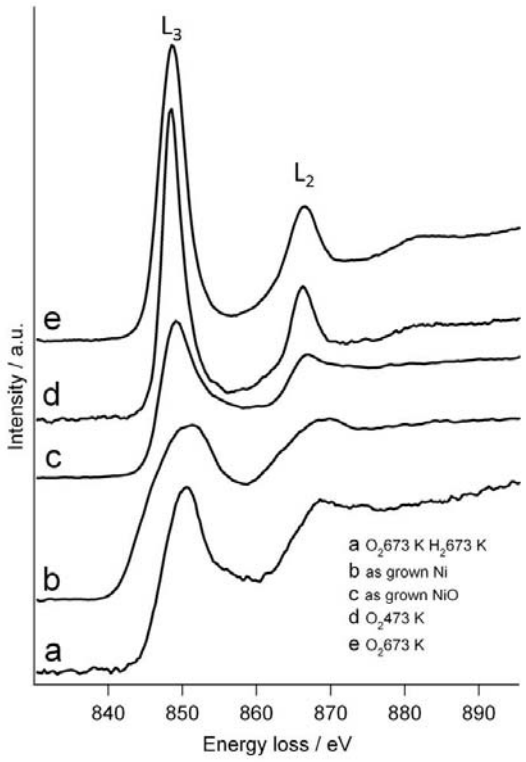
L3
L2
e
d
c
b
a
Intensity / a.u.
a O2673 K H2673 K
b as grown Ni
c as grown NiO
d O2473 K
e O2673 K
840
850
860
870
880
890
Energy loss / eV

Figure 8

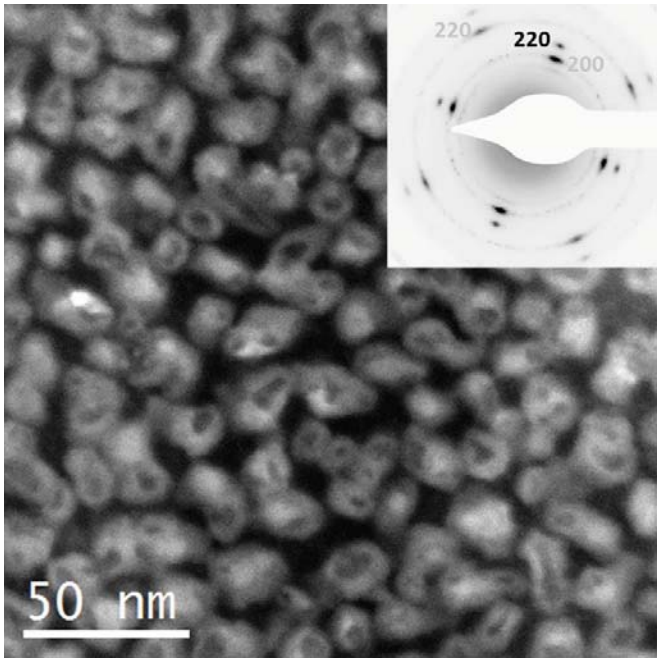

Figure 9

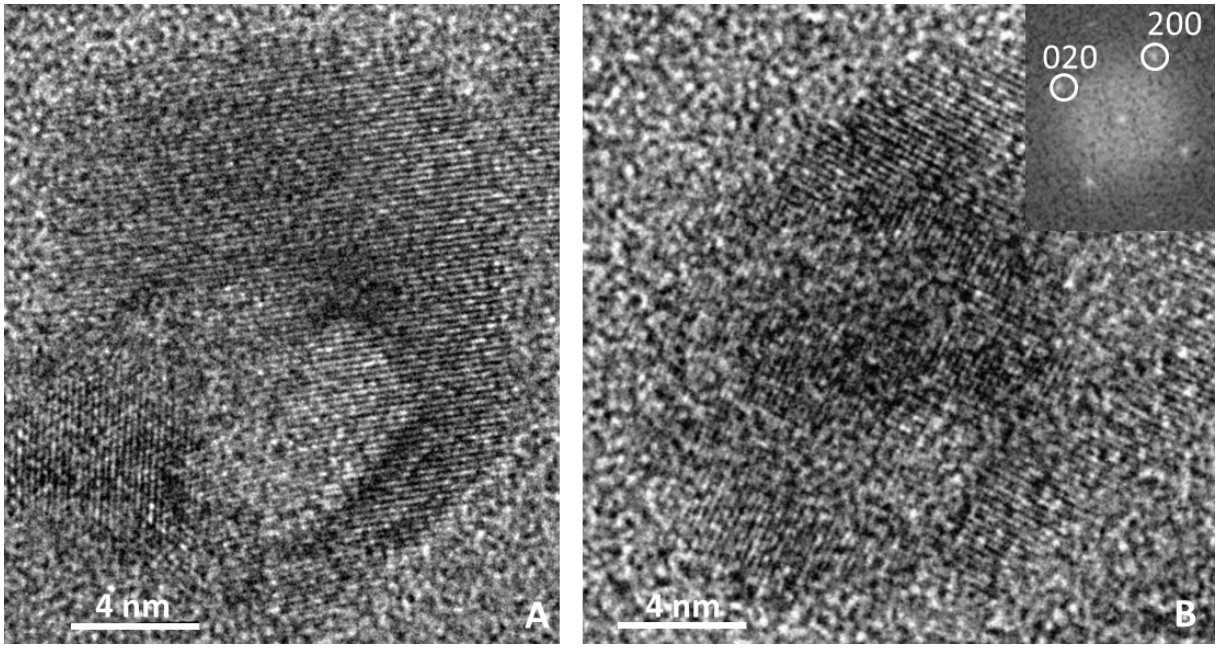

Figure 10

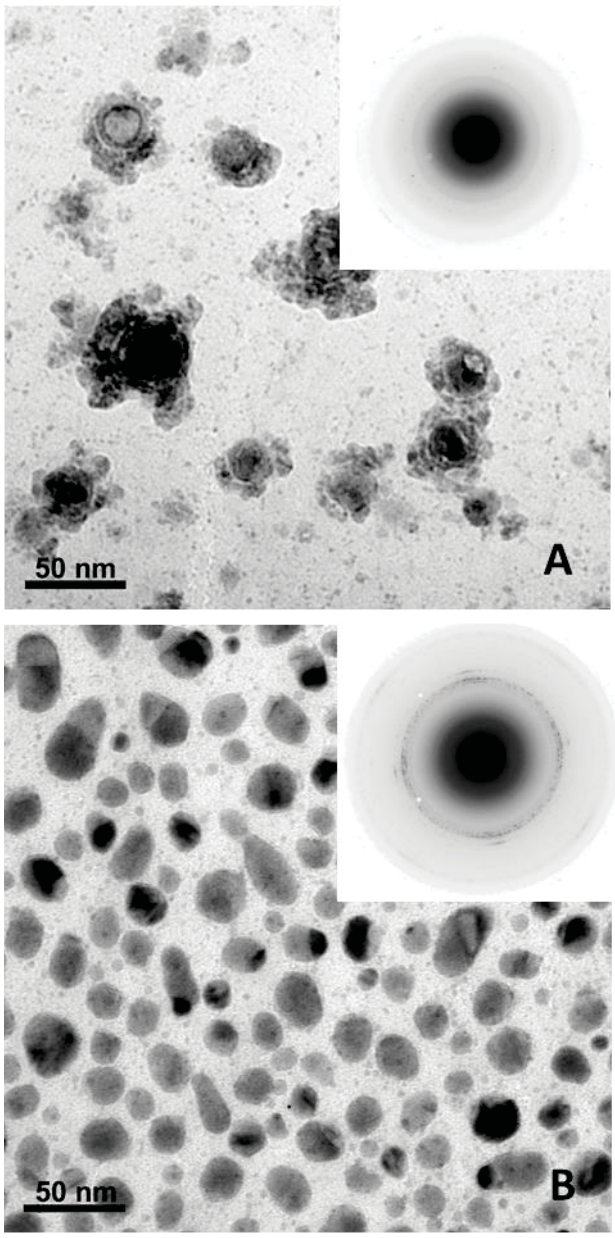

Figure 11

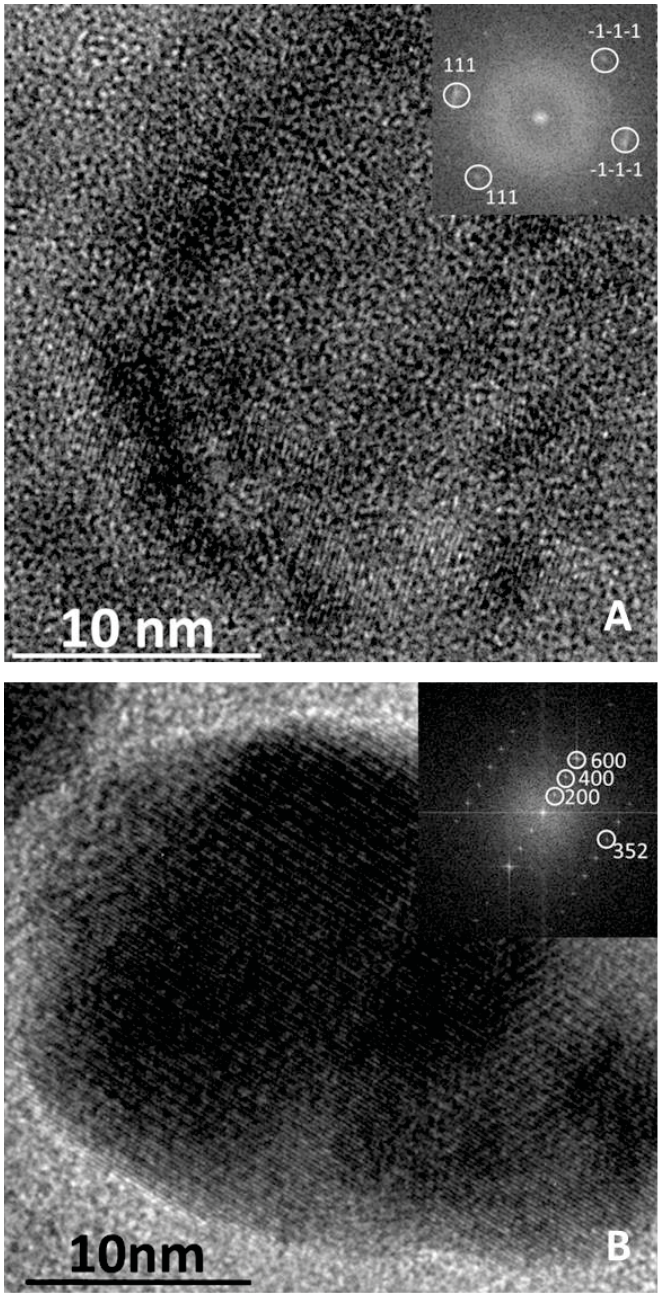

Figure 12